Research Article

Journal of Environmental Nanotechnology

Environmentally Sustainable Optimization of Plasma Spray Technique for Chromium Oxide Coatings on SS306 Steel

S. Sabanayagam[1*], M. Kumaresan[2], O. A. Sridevi[3] and P. Srinivasan[4]

[1]Department of Mechanical Engineering, Kings College of Engneering, Punalkulam, TN, India
[2]Department of Chemistry, Nehru Institute of Technology, Coimbatore, TN, India
[3]Department of Chemistry, Karpagam Institute of Technology, Coimbatore, TN, India
[4]Department of Mechanical Engineering, Periyar Maniammai Institute of Science and Technology, Vallam, Thanjavur, TN, India
Received: 05.08.2025 Accepted: 11.09.2025 Published: 30.09.2025
*sundaramsabanayagam@gmail.com

ABSTRACT

This study investigates the plasma spray coating of chromium oxide nanoparticles (nCr_2O_3) on SS306 stainless steel substrates to enhance surface performance, addressing the growing demand for elevated-temperature, wear resilience coatings in engineering uses. Utilizing a Taguchi L9, the impact of key process parameters, *viz*., plasma arc current (PAC), plasma gas flow rate (PGFR), carrier gas flow rate (CGFR), and spray distance (SD), were optimized using desirability function. ANOVA test revealed SD as the most influential factor for micro-Vickers hardness ($p = 0.0027$) and % porosity ($p = 0.0109$). Optimal parameters (PAC = 500 A, PGFR = 40 L/min, CGFR = 2 L/min, SD = 100 mm) resulted in a maximum predicted hardness of 726.58 HV and minimum porosity of 3.24%. A confirmation trial showed a 1.27% increase in hardness and a 4.52% reduction in porosity over predicted values. Formation of a dense, homogenous coating with minimal surface defects was confirmed by SEM analysis. The integration of nCr_2O_3 with optimized process parameters significantly enhances coating quality through improved particle melting, splat formation, and grain boundary strengthening.

Keywords: Plasma spray coating; Taguchi's DoE; Desirability function; Micro-hardness; Porosity; Nano Cr_2O_3.

1. INTRODUCTION

Surface modification through thermal spray coatings has developed as a crucial technique for improving the functional efficiency of engineering materials subjected to extreme service conditions, including intense heat, corrosion, and wear (Lakkannavar *et al*. 2024). Various coating techniques are employed in surface engineering to enhance material properties, including electroplating, physical vapor deposition (PVD), high-velocity oxy-fuel (HVOF) spraying, chemical vapor deposition (CVD), and thermal spray approaches like flame/plasma/arc spraying. Among these, plasma spray coating stands out for its capability of depositing wider materials like ceramics, metals, and composites onto diverse substrates with high deposition rates and thick, dense coatings (Bolelli *et al.* 2021). Unlike CVD and PVD, which typically produce thin films and require vacuum environments, plasma spray operates at atmospheric pressure and can form thicker coatings suitable for industrial wear and thermal barrier applications. Compared to HVOF or flame spraying, plasma spray offers much higher particle temperatures (up to 15,000 K), enabling even high-melting-point materials like oxides to be effectively melted and deposited. A major advantage of plasma spray is its flexibility in material selection and ability to coat large or complex-shaped components with excellent mechanical bonding (Martin *et al*. 2019).

Furthermore, the use of nanosized particles instead of micron-sized powders in plasma spray coatings has shown significant benefits. Nanoparticles have a greater ratio of surface area to volume, which enhances melting efficiency, leads to better particle flattening upon impact, and promotes denser, finer-grained microstructures. This results in coatings with higher hardness, improved wear resistance, and lower porosity, offering superior performance compared to coatings made with conventional micron-sized powders. Thus, combining plasma spray with nanoceramic powders presents a promising route for developing next-generation functional coatings for critical engineering applications. Plasma spray coating parameters are important in defining the quality, structure, and efficiency of the deposited coating. The key variables, such as plasma arc current (PAC), plasma gas flow rate (PGFR), carrier gas flow rate (CGFR), powder feed rate, torch traverse speed and spray distance (SD) directly influence the kinetic and heat energy imparted to the feedstock particles (Kengesbekov *et al.* 2024). These process parameters dictate the degree of particle flattening, coating thickness, porosity, and microhardness, making

their optimization essential for achieving coatings with superior mechanical integrity and surface quality.

2. LITERATURE REVIEW AND OBJECTIVES

Sun *et al.* (2025) developed *in situ* particle-strengthened Cu-based composite coatings using submicron TiC and nano-Ti_xO (x = 1, 2) through reactive plasma spraying. Coatings reinforced with TiC and Ti_xO particles outperform CuCrZr alloy in hardness and durability to wear. Coatings mostly experience adhesive wear while CuCrZr alloy primarily experiences oxidation wear. Using powders of titanium and zinc, Deng *et al.* (2025) fabricated plasma sprayed (Ti,W)N composite coatings. These composite coatings consisted of solid solutions of TiN, W_2N, TiO_2, W, and (Ti,W)N. Nanocrystals made up the grains, doping W made the coating denser and gave it more micro-hardness. Doping 25 wt.% W powders into a (Ti,W)N coating increased its micro-hardness from TiN to 1332 HV, a 43% improvement. After using plasma-influenced high-velocity arc spraying technique to develop Inconel 625 metal coatings and an Inconel 625-Al_2O_3 composite coating, Jiang *et al.* (2025) subjected the coating to high heat oxidation at 800°C. It was noted that the Inconel 625-Al_2O_3 composite coating performs extremely well at room temperature. However, when subjected to high-temperature oxidation, the porosity of the coating drops by 16.71%, while the hardness and elastic modulus rises by 9.6% and 27.8%, respectively. This is because the coating generates circular chromium oxide nano particles (nCr_2O_3), which can greatly strengthen it and decrease defects. By using high-speed ball milling for pre-mixing and embedding treatment, Zhou *et al.* (2025) were able to develop a micro-nano SiC/6061Al coating. Metallurgical bonding takes place in the particle border areas of the composite coating following solid solution treatment (500°C, 4 h). Nano SiC reacts with Al to produce Al_9Si strengthening phases. Using a solution to treat the SiC/6061Al composite coating raised its elastic modulus by 13.17% and nano hardness of the 6061Al particle areas by 45.42% compared to the coating that did not undergo solution treatment.

Using the suspension plasma spraying (SPS) process, Huang *et al.* (2025) examined the effectiveness of an yttria-stabilized zirconia thermal barrier coating over a smooth β-(Ni,Pt)Al bondcoat due to the ceramic topcoat and the very thick α-Al_2O_3 layer, the inter-diffusion of Al played a crucial role in the bondcoat phase transition. Thermal barrier coatings (TBCs) that used an SPS VC topcoat and a β-(Ni,Pt)Al bondcoat outperformed traditional air plasma spray (APS) TBCs in terms of thermal cycling and shock life, with values of 1500 and 557 times higher, respectively. The spraying settings control the porosity formation and growth on plasma-sprayed coatings. The best coatings with the fewest defects were achieved by using optimized set spraying settings. The way plasma-sprayed coatings adhere and stay together depends on factors including the shape and size of splats, the shape of cracks, and porosity. The ability of coating to trap gas affects its thermal behaviour in TBC (Odhiambo *et al.* 2019). Hervy *et al.* (2025) defined wide parametric window for achieving columnar YSZ TBCs *via* axial solution precursor plasma spraying, that achieved SPS-comparable columnar microstructure under specific parameters. Relevant deposition rates with enhanced microhardness were noticed. Solution precursor plasma spraying coatings showed better erosion. Nie *et al.* (2025) fabricated self-lubricating Mo and BN reinforced NiCr coatings by APS. The deposition efficiency and coating structure were affected by the flow of H_2. The friction film on the sliding surface enhanced the wear resilience of the coating. The transition of the wear mechanism with changes in the H_2 flow rate was elucidated. The primary form of wear changed as the H_2 flow rate increased, moving from adhesive wear which produced significant material transfer to grinding ball cutting which generated furrow wear. Morelli *et al.* (2025) fabricated coatings made of 8YSZ with aggregated and sintered, fused and crushed, or hollow spherical precursor powders. They were investigated for their thermal conductivity in two states: as-deposited and upon thermal cycling. Porosity decreases after thermal cycling, increasing thermal conductivity. Thermal conductivity of bilayer coatings depends on top layer porosity, not on Y_2O_3 content. It was noted that 8YSZ has higher fracture toughness than 20YSZ and 55YSZ coatings. Cellard *et al.* (2009) developed Cr_2O_3 fused crushed powders and nCr_2O_3 coatings by plasma spray having grains size of 100 nm. Research has shown that granulated nCr_2O_3, having a granulometric dispersion ranging from 20 to 63 µm, may enhance the resilience to wear of coatings. Coatings made using nanostructured materials have a wear resistance 20 times greater than that of coatings made with micrometric powder, primarily owing to their unique microstructure.

Chromium oxide, a hard, chemically inert, and thermally stable ceramic, is widely used in protective coatings owing to its excellent corrosion and wear resilience and hardness (Manojkumar *et al.* 2025). With the advancement in nanotechnology, the incorporation of chromium oxide (nCr_2O_3) nanoparticles has shown promise in further improving coating characteristics attributable to the larger surface area and better packing density of nanoparticles. However, deposition of thick, defect-free coatings with optimized properties requires precise control over plasma spray parameters, which significantly influence coating adhesion, microstructure, and mechanical characteristics (Hango *et al.* 2024).

This study focuses on the application of nCr_2O_3 coatings on Stainless Steel 306 (SS306) substrates using plasma spray technique, aiming to improve surface hardness and minimize porosity; two critical indicators of coating performance. Stainless steel 306, though

widely used for its corrosion resistance and formability, lacks the surface hardness required in highly abrasive or thermal environments. This work employs a Taguchi L9 orthogonal array to systematically optimize key process parameters PAC, PGFR, CGFR, and SD to obtain superior coating characteristics with minimal experimentation. Furthermore, the study integrates statistical modeling (ANOVA), response optimization (desirability analysis), and microstructural evaluation (SEM) to comprehensively understand the correlation between process inputs and coating quality. The optimized coating exhibited enhanced micro-Vickers hardness and significantly reduced porosity, demonstrating the efficacy of nano-ceramic reinforcement in extending the functional lifespan of SS306 components in demanding applications.

3. MATERIALS AND METHODS

3.1 Stainless Steel 306

Stainless Steel 306 is an austenitic stainless steel renowned for its exceptional resistance to corrosion, moderate strength, and excellent formability. Physically, it has a density of approximately 7.9 g/cm^3 and exhibits a smooth, metallic surface finish. Thermally, it has a melting range of 1370–1400°C and a thermal conductivity of around 16.3 W/mK, which is relatively low compared to other metals, making it moderately resistant to heat transfer (Schino, 2020). Mechanically, SS306 offers a tensile strength of about 515 MPa and good elongation and ductility, suitable for wider structural and industrial uses. However, in aggressive environments involving high wear, extreme temperatures, acidic or corrosive media, the surface properties of SS306 may degrade over time (Vakili *et al.* 2024). Coating SS306 with ceramic particles in micron and nano size significantly enhances its surface hardness, wear and oxidation resilience, and thermal barrier capabilities, without compromising its core structural integrity. This is especially beneficial in fields like chemical processes, power production, and aerospace, where long-term durability, resistance to surface degradation, and reduced maintenance are critical (Chate *et al.* 2023).

3.2 Chromium Oxide Nanoparticles

Chromium oxide Nanoparticles possess exceptional physical, thermal, and mechanical properties that make them highly suitable for use as a coating material, particularly in high-performance and harsh environments. Physically, nCr_2O_3 exhibits a high density (5.22 g/cm^3) and fine grain structure, which contribute to forming compact and uniform coatings with low porosity (Mao *et al.* 2022). Thermally, it offers excellent heat stability and a high melting point (over 2435°C), ideal for thermal barrier applications and environments with extreme temperature fluctuations. Mechanically, nCr_2O_3 is characterized by its outstanding hardness (comparable to corundum), wear resistance, and chemical inertness, which protect substrates from abrasion, corrosion, and oxidative degradation (Xiong *et al.* 2020). Compared to other ceramic particulates *viz*., zirconia (ZrO_2), titania (TiO_2), alumina (Al_2O_3), nCr_2O_3 coatings provide superior corrosion resistance, especially in acidic and high-temperature conditions, and exhibit stronger adhesion due to their fine particle size and improved surface contact (Kiilakoski *et al.* 2019). Additionally, the unique green color and optical properties of nCr_2O_3 are beneficial for specialized aesthetic and infrared applications.

3.3 Plasma Spray Coating Technique

The schematic diagram (Fig. 1) illustrates plasma spray coating process conducted in a controlled atmosphere chamber designed to deposit nCr_2O_3 particles onto an SS306 stainless steel substrate. In this setup, nitrogen (N_2) was used as the plasma gas supplied near the electrode region and ionized by an electric arc generated between cathode and anode. This ionization produces a high-energy plasma jet that exits through a nozzle. Then, nCr_2O_3 powder was fed into the plasma stream using argon as the carrier gas due to its inert nature, which prevents unwanted chemical reactions. As the nano-sized particles are entrained into the plasma jet, they become semi or fully molten and are driven at high velocity to the substrate. The substrate (SS306), receives these particles, which flatten and solidify upon impact to form a dense, adherent coating. The entire process was carried out in vacuum or controlled atmospheric conditions to ensure coating purity and consistency. Cold water was allowed to flow around the torch components to maintain temperature stability. This method is highly effective for forming hard, wear-resistant coatings with excellent corrosion protection on metallic components (Thirugnanasambandam *et al.* 2025). In this study, plasma spray coating was performed with different combinations of PAC, PGFR, CGFR, and SD.

Taguchi's Design of Experiments (DoE) using the L9 orthogonal array is an efficient method to study the influence of multiple parameters on a system with significantly fewer experimental runs. Specifically, the L9 array is suitable for analyzing four parameters (PAC, PGFR, CGFR, and SD), each varied through three levels, requiring only nine experimental trials instead of 81 in a full factorial design. This structured matrix allows each level of every parameter to be tested equally and independently, ensuring a balanced evaluation of main effects. The L9 array enables researchers to identify the optimal combination of parameter levels by analyzing the results using means which helps in enhancing performance and minimizing variability (Chakravarthy *et al.* 2023).

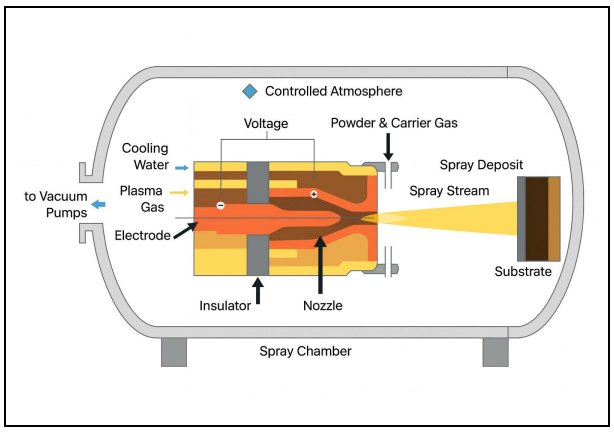


Fig. 1: Graphical view of plasma spray coating

3.4 Characterization

The micro-Vickers hardness of a coated substrate was determined by subjecting the polished cut surface of the coating to indentation using a diamond pyramid-shaped indenter under a controlled load (500 g) and dwell time (10 seconds), following the guidelines of ASTM E384. Multiple indentations were made across the coated region at fixed intervals to obtain an average value and assess uniformity (Factor and Roman, 2000). The % porosity of the coating on the substrate was determined using SEM taken on the cross-sectional micrographs of the coated layer. After coating, the coated sample was sectioned, mounted, refined and etched to expose the microstructure in a distinctive way. High-resolution SEM images captured were analyzed using image processing software (ImageJ), where the dark regions (pores) and bright regions (solid coating) are distinguished based on grayscale thresholds. The software calculates the area fraction of pores relative to the total coating area, which is then expressed as a percentage, known as % porosity (Thilagashanthi *et al.* 2021).

4. RESULTS AND DISCUSSIONS

4.1 Modelling and Optimization

After performing the plasma spray coating on the substrate of SS306 with nCr_2O_3 as per the L9 array, micro-Vickers hardness and % porosity were determined as tabulated in Table 1. The results indicate that increasing PAC from 400 A to 600 A generally improves coating hardness, with the highest microhardness of 722.8 HV observed at 600 A (Trial 8), likely due to better melting and acceleration of nCr_2O_3 (Zhou *et al.* 2024). Similarly, PGFR plays a crucial role in thermal energy delivery and coating adhesion. Moderate flow rates (e.g., 40 L/min) yielded relatively higher hardness and lower porosity. Carrier gas flow rate influences particle transport and dispersion; optimal values (around 4 L/min) seem to enhance uniform deposition, as seen in trials with low porosity like Trial 4 (3.1%) (Feng *et al.* 2007). Spray distance significantly affects nCr_2O_3 solidification; an SD of 100 mm appears favorable for hardness, possibly due to optimal particle flattening, whereas shorter SD might cause increased porosity because of incomplete melting. Overall, the combination of high PAC (600 A), moderate PGFR and CGFR, and longer SD (100 mm) enhances coating density and microhardness, while reducing porosity thus enhancing the protective efficiency of the ceramic coating on SS306 (Chinnusamy *et al.* 2019).

Table 1. L9 Taguchi array with outputs

Trial No.	PAC (A)	PGFR (L/min)	CGFR (L/min)	SD (mm)	Microhardness (HV)	Porosity (%)
1	400	30	2	80	627.4	4.1
2	400	40	4	90	680.8	3.6
3	400	50	6	100	700.3	3.8
4	500	30	4	100	710.9	3.1
5	500	40	6	80	670.2	3.8
6	500	50	2	90	698.7	3.4
7	600	30	6	90	685.4	3.2
8	600	40	2	100	722.8	3.5
9	600	50	4	80	665.5	4.3

For analyzing and modelling the outputs, ANOVA needs to be performed to check for statistical significance. In the presented Taguchi L9 dataset with four control factors (PAC, PGFR, CGFR, SD) each at three levels, and only 9 experimental trials, a standard ANOVA cannot be directly applied due to zero degrees of freedom (DoF) for error. To overcome this, pooling ANOVA is employed. In pooling ANOVA, the least significant factors (those with minimal sum of squares and presumed negligible effect on the output) are pooled into the error term (Shabani *et al.* 2023). This provides a realistic estimate of the experimental error variance and allows the calculation of F-ratios to test the significance of the remaining factors. Pooling improves the robustness of ANOVA when dealing with limited experimental runs, enabling proper ranking and significance assessment of the remaining influential process parameters.

Table 2 and Table 3 present the ANOVA results for micro-hardness and % porosity data. In both the cases, during pooling it is found that the CGFR is least significant and hence, it is considered the error variance and obviously the error DoF is 2. The ANOVA results for micro-Vickers hardness reveal that the developed model is extremely significant, with a model F-value of 161.616 and a corresponding p-value of 0.0062, seeming to suggest a robust statistical association among input process parameters and the hardness. Among the factors considered, SD emerged as the most influential parameter, exhibiting the highest F-value of 370.838 and

a highly significant p-value of 0.0027, suggesting that variations in SD greatly affect coating hardness (Pannerselvam, 2012). This is followed by PAC and PGFR both of which are also statistically significant contributors. The model exhibits excellent goodness-of-fit indicators: R^2 = 0.9979, Adjusted R^2 = 0.9918, and Predicted R^2 = 0.9583, all of which are in close agreement, demonstrating the model's robustness and high predictive competence. The low coefficient of variation (CV=0.376%) further confirms the precision and reproducibility of the data, while the adequate precision value of 41.969 far exceeds the acceptable limit of 4, confirming a strong signal-to-noise ratio.

Table 2. Micro-vickers hardness ANOVA data

Source	SS	DoF	MSS	F-value	p-value	
Model	6441.993	6	1073.666	161.616	0.0062	significant
PAC	1041.327	2	520.6633	78.374	0.0126	
PGFR	473.46	2	236.73	35.634	0.0273	
SD	4927.207	2	2463.603	370.838	0.0027	
Residual	13.28667	2	6.643333			
Cor Total	6455.28	8				
Std. Dev.	2.577466		R^2	0.9979		
Mean	684.6667		Adjusted R^2	0.9918		
CV %	0.376456		Predicted R^2	0.9583		
			Adeq Precision	41.969		

Table 3. % Porosity ANOVA data

Source	SS	DoF	MSS	F-value	p-value	
Model	1.253	6	0.209	47	0.0209	significant
PAC	0.242	2	0.121	27.25	0.0354	
PGFR	0.202	2	0.101	22.75	0.0421	
SD	0.809	2	0.404	91	0.0109	
Residual	0.009	2	0.004			
Cor Total	1.262	8				
Std. Dev.	0.067		R^2	0.9929		
Mean	3.644		Adjusted R^2	0.9718		
CV %	1.829		Predicted R^2	0.8574		
			Adeq Precision	20.41		

The pooled ANOVA results for % porosity, as shown in Table 3, demonstrate that the developed model is very significant (F=47, p=0.029), suggesting that the chosen process parameters have a meaningful influence on the porosity of the coated substrate. Among the input factors, SD has the most substantial impact, as evidenced by the highest F-value of 91 and the lowest p-value of 0.0109, confirming its critical role in controlling coating density and pore formation (Cai *et al.* 2014). The parameters, PAC and PGFR are also significant contributors, with F-values of 27.25 and 22.75, and p-values of 0.0354 and 0.0421, respectively, indicating their strong but relatively lesser influence compared to SD. The very low residual error (0.009) suggests minimal variation in the data. The model's performance metrics further support its reliability, with an exceptionally high R^2 value of 0.9929, adjusted R^2 of 0.9718, and predicted R^2 of 0.8574, all of which are in good agreement, indicating strong model accuracy and predictive capability. The low CV (1.829%) and standard deviation (0.067) further confirm the high precision and repeatability of the experimental results.

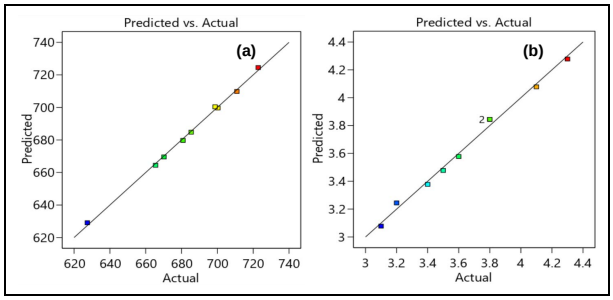


Fig. 2: Predicted vs. actual plot (a) Micro-hardness and (b) % porosity

Fig. 2 presents the diagnostic plot for the outputs. The predicted *vs*. actual plots for micro-hardness and % porosity, validate the robustness and accuracy of the developed regression models used in the analysis. In the case of micro-hardness (Fig. 2a), the data points are closely aligned along the 45° line, representing a robust correlation among experimental values and the model's predictions. This alignment confirms minimal deviation and high predictive accuracy, which is further supported by the higher R^2 value of 0.9979 and low standard deviation observed in the ANOVA analysis (Zhang *et al.* 2024). Similarly, for % porosity (Fig. 2b), the predicted values show excellent agreement with the actual experimental data, as majority of the data points are located close to the diagonal. with very small scatter. This consistency establishes the model's capability to precisely capture the variation in porosity based on process parameters. The high R^2 value of 0.9929 and low residual error observed in the ANOVA table for porosity further reinforce this conclusion.

The interaction plots and 3D surface graphs presented in Fig. 3 for micro-Vickers hardness clearly illustrate how the combined effects of plasma spray parameters influence the coating hardness of nCr_2O_3 on SS306. The interaction plot between PAC and PGFR shows that microhardness increases with higher PAC and PGFR values, with the combination of 500 A PAC and 50 L/min PGFR yielding superior results. A more prominent trend is seen in the PAC *vs*. SD plot, where an increase in SD significantly improves hardness, especially at 100 mm SD and 500 A PAC, indicating optimal particle melting and impact velocity (Patel *et al.* 2022). The PGFR *vs*. SD plot further reinforces that 100 mm SD consistently yields higher hardness across all PGFRs, with the highest values appearing at 50 L/min PGFR.

These trends are further supported by the 3D bar plots, where the maximum microhardness values are visually observed at combinations involving high SD and mid-to-high PAC and PGFR values (Abbas *et al.* 2021). Notably, the red bars (short SD or low PAC/PGFR) show lower hardness, while blue bars (long SD or optimal energy input) show peak hardness performance.

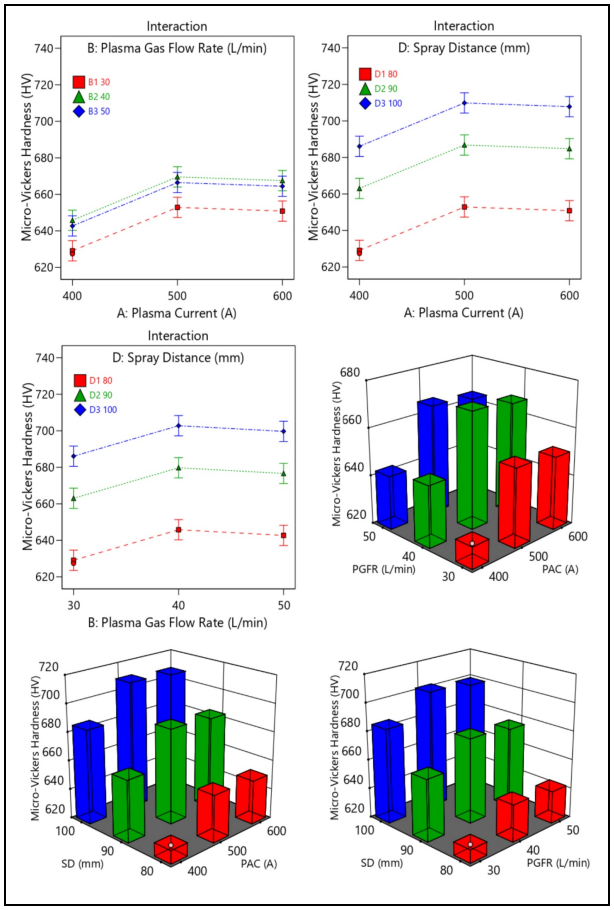


Fig. 3: Interaction plot and 3D plot for micro-Vickers hardness

Fig. 4 presents the interaction plot between PAC and PGFR. It reveals that porosity generally decreases at 500 A, particularly when PGFR is moderate (40 L/min), indicating improved melting and deposition behaviour. A similar trend is observed in the interaction between PAC and SD, where porosity reaches its lowest value around 500 A and 90 mm SD, suggesting this combination yields optimal particle heating and flight time (Kar *et al.* 2018). The PGFR *vs*. SD interaction plot further highlights that longer SDs (90-100 mm) combined with moderate PGFR reduce porosity, likely due to better particle flattening and reduced splattering. The 3D surface plots corroborate these trends visually; lower porosity is represented by shorter bar around 500 A PAC, 40 L/min PGFR, and 90 mm SD. Notably, higher porosity levels are consistently associated with either too short a SD (80 mm) or extreme PGFR (30 or 50 L/min), emphasizing the sensitivity of the coating quality to parameter balance (Liu *et al.* 2025).

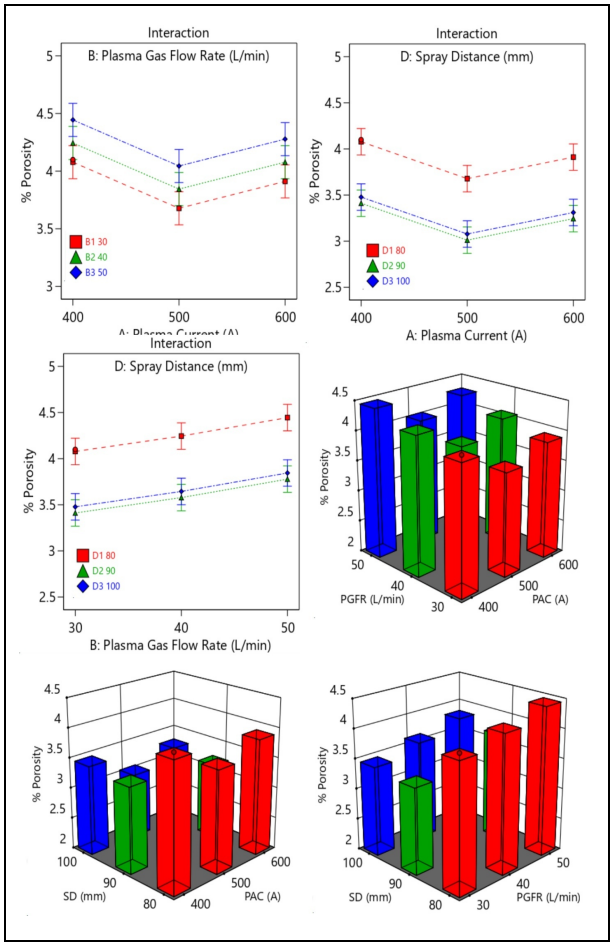


Fig. 4: Interaction plot and 3D plot for % porosity

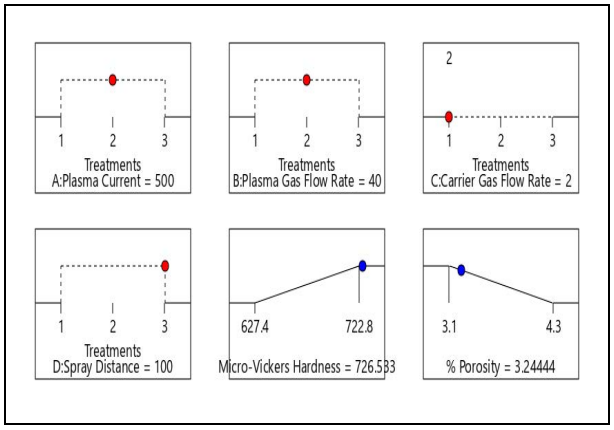


Fig. 5: Ramp plot showing optimal conditions

Fig. 5 presents the ramp plot for multi-criteria optimization: maximizing micro-Vickers hardness and minimizing porosity using desirability approach. The solution, which has a high overall desirability of 0.938, indicates that the best outcome is achieved when the PAC is set to 500 A, PGFR to 40 L/min, and SD to 100 mm with the non-significant CGFL at 2 L/min. These settings collectively lead to a predicted micro-Vickers hardness of 726.58 HV, which is near the maximum observed value

in the experimental data, and a reduced % porosity of 3.24%, which is close to the lower range of recorded values. The desirability close to 1 reflects an excellent balance between hardness enhancement and porosity reduction (Du *et al.* 2020).

The desirability plot presented in Fig. 6 provides a visual summary of how well the selected input parameters satisfy the optimization goals for maximizing micro-Vickers hardness and minimizing % porosity. All the input parameters have a default desirability value of 1, whereas output micro-Vickers hardness achieves a desirability of 1, successfully predicting the maximum possible hardness value within the experimental range.

The % porosity achieves a desirability of 0.87963, which, while not perfect, still reflects a strong minimization of porosity under the given conditions. The combined desirability score of 0.937886 confirms that the selected solution offers a highly optimized trade-off between enhancing hardness and minimizing porosity, thereby ensuring an effective and reliable coating process configuration (Mohankumar *et al.* 2022).

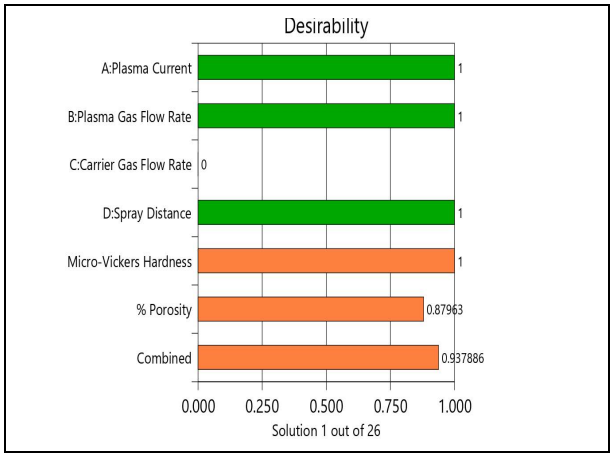


Fig. 6: Desirability plot showing individual and combined values

Fig. 7 presents the desirability values predicted for various combinations of input parameters. A desirability scores closer to 1 indicates a more favorable combination of parameters that simultaneously maximize micro-Vickers hardness and minimize porosity. In PAC *vs*. PGFR plot, the highest desirability is achieved at 500 A PAC and 40 L/min PGFR, confirming this as an optimal setting. The PAC *vs*. SD plot reveals that the combination of 500 A and 100 mm SD yields the most desirable outcome, while lower currents (400 A) and SDs (80 mm) result in significantly lower desirability. The PGFR *vs*. SD plot also highlights 40 L/min PGFR and 100 mm SD as the most favorable settings, again reflecting high desirability values near 0.9. In contrast, combinations involving low PGFR (30 L/min) and short SD (80 mm) consistently produce low desirability, indicating suboptimal performance in terms of hardness and porosity. Overall, moderate to high values of PAC (500 A), PGFR (40 L/min), and SD (100 mm) work synergistically to produce nCr_2O_3 coating on SS306 substrate with superior mechanical integrity and low porosity, achieving near-ideal desirability.

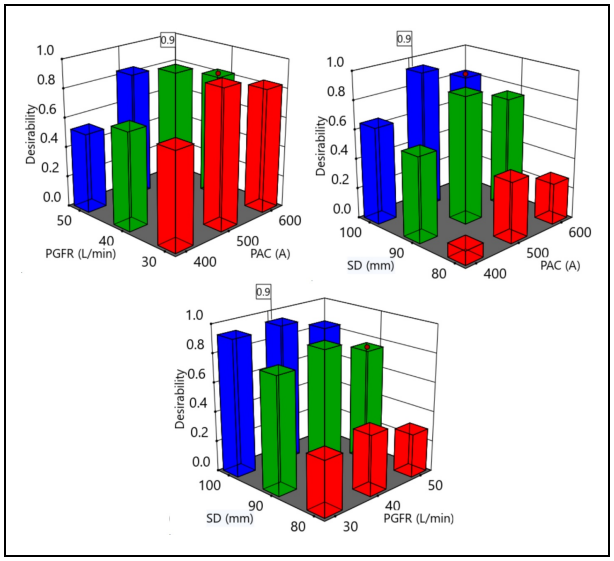


Fig. 7: Variation of desirability values with change in inputs

4.2 Microstructural Analysis

The SEM micrographs in Fig. 8 provide detailed insights into the surface morphology of nCr_2O_3 ceramic coatings deposited on SS306 under different trial settings from the L9 Taguchi array. Trial 1, with the lowest microhardness (627.4 HV) and relatively high porosity (4.1%), exhibits a rough and irregular surface with numerous voids and incomplete particle fusion, likely due to insufficient particle melting and low impact velocity resulting from low PAC (400 A), low PGFR (30 L/min), and short SD (80 mm) (Prashar *et al.* 2024). Trial 3, which shows moderate hardness (700.3 HV) and porosity (3.8%), presents a smoother and more stratified morphology, indicating better molten particle spreading due to improved energy input at higher SD (100 mm) and PGFR (50 L/min), despite low PAC. Trial 5 has a hardness of 670.2 HV and porosity of 3.8%, and the microstructure displays compact lamellar features, yet with signs of inter-splat boundaries and partial unmelted particles, possibly due to suboptimal SD (80 mm) at mid-level PAC and PGFR (Kebriyaei *et al.* 2024). In contrast, Trial 6, with higher hardness (698.7 HV) and lower porosity (3.4%), reveals a relatively smooth and dense coating with fewer defects, indicating efficient melting and impact of particles under optimized PAC (500 A) and increased SD (90 mm). Trial 9, having moderate hardness (665.5 HV) but the highest porosity (4.3%), shows a porous and uneven microstructure, indicating poor cohesion between splats, likely caused by excessive CGFR (4 L/min) and short SD (80 mm), which may have led to premature cooling and splatter (Samal *et al.* 2023).

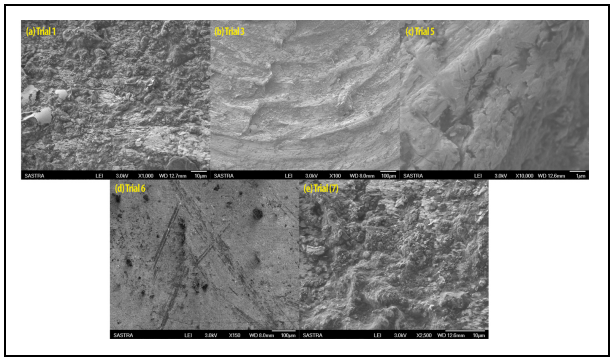


Fig. 8: SEM micrographs of coated surface

From the identified optimal conditions of PAC 500 A, PGFR 40 L/min, CGFL 2 L/min, and SD 100 a confirmation experimental was planned with the same experimental procedure and the outputs obtained were; % porosity of 3.1%, and micro-Vickers hardness of 735.9 HV. When compared with the predicted values of 726.58 HV, and 3.24 % porosity, the confirmation experiment produces 1.27 % higher micro-hardness and 4.52 % lower porosity proving the supremacy of the optimal condition. Fig. 9 presents the surface SEM of optimal setting; the microstructure reveals a uniform, dense, and well-adhered coating surface with minimal surface defects and splat boundaries, indicating excellent particle melting and deposition characteristics. The surface appears smooth with very few pores or uncoated areas, which correlates with the observed 4.52% reduction in porosity compared to the predicted value, affirming effective particle flattening and inter-splat cohesion (Vaßen *et al.* 2023). Additionally, the absence of cracks, large voids, or delamination features supports the recorded 1.27% improvement in micro-Vickers hardness, suggesting enhanced densification and stronger particle-substrate bonding.

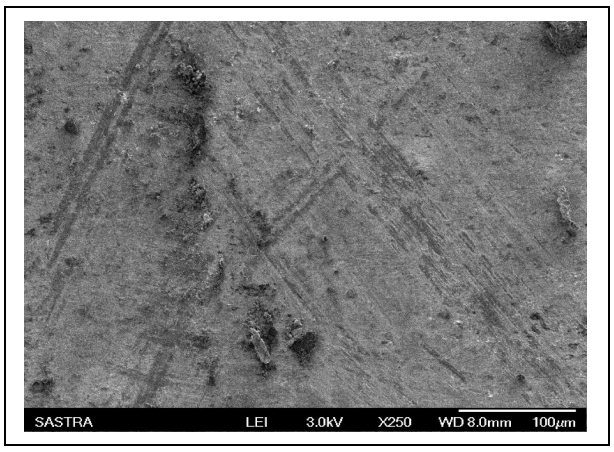


Fig. 9: SEM picture of optimal setting

5. CONCLUSION

Based on the experimental results, statistical analysis, and microstructural evaluation, the plasma spray coating of nCr_2O_3 on SS306 substrate significantly enhanced micro-Vickers hardness and reduced porosity. ANOVA results confirmed that SD, and PAC were the most influential factors for hardness, while SD also dominated in porosity reduction. The optimal parameter combination (PAC = 500 A, PGFR = 40 L/min, CGFR = 2 L/min, SD = 100 mm) yielded a predicted microhardness of 726.58 HV and porosity of 3.24%, which were further validated in the confirmation test with a 1.27% higher hardness and 4.52% lower porosity than predicted. The enhanced hardness is attributed to the improved kinetic energy and thermal input delivered to the nCr_2O_3 particles at optimal PAC and PGFR, ensuring complete melting and accelerated impact on the substrate. This results in better splat flattening, densification, and strong inter-splat bonding, forming a cohesive and mechanically robust coating layer. Additionally, the longer SD (100 mm) provides adequate flight time for the particles to melt uniformly and decelerate slightly before deposition, reducing porosity caused by rebound or splashing. The nCr_2O_3 also contributes to hardness improvement through a grain boundary strengthening mechanism, while reduced porosity enhances load-bearing capacity and prevents crack initiation. The SEM analysis confirmed these mechanisms, revealing a dense, uniform, and pore-free coating morphology under optimized conditions.

FUNDING

This research received no specific grant from any funding agency in the public, commercial, or not-for-profit sectors.

CONFLICTS OF INTEREST

The authors declare that there is no conflict of interest.

COPYRIGHT

This article is an open-access article distributed under the terms and conditions of the Creative Commons Attribution (CC BY) license (http://creativecommons.org/licenses/by/4.0/)

REFERENCES

Abbas, R. A., Ajeel, S. A., Bash, M. A. A. and Kadhim, M. J., Effect of Plasma Spray Distance on the Features and Hardness Reliability of YSZ Thermal Barrier Coating, *Mater. Today Proc.,* 42, 2553–2560 (2021). https://doi.org/10.1016/j.matpr.2020.12.578

Bolelli, G., Steduto, D., Kiilakoski, J., Varis, T., Lusvarghi, L. and Vuoristo, P., Tribological Properties of Plasma Sprayed Cr_2O_3, Cr_2O_3–TiO_2, Cr_2O_3–Al_2O_3 and Cr_2O_3–ZrO2 Coatings, *Wear.,* 480–481, 203931(2021)., https://doi.org/10.1016/j.wear.2021.203931.

Cai, Z., Deng, S., Liao, H., Zeng, C. and Montavon, G., The Effect of Spray Distance and Scanning Step on the Coating Thickness Uniformity in Cold Spray Process, *J. Therm. Spray Technol.,* 23(3), 354–362(2014). https://doi.org/10.1007/s11666-013-0002-0

Cellard, A., Garnier, V., Fantozzi, G., Baret, G. and Fort, P., Wear Resistance of Chromium Oxide Nanostructured Coatings, *Ceram. Int.,* 35(2), 913–916(2009). https://doi.org/10.1016/j.ceramint.2008.02.022

Chafjiri, Z. S., Zadeh, A. A., Seraj, R. A. and Azarniya, A., Effect of Cold Spray Processing Parameters on the Microstructure, Wear, and Corrosion Behavior of Cu and Cu–Al_2O_3 Coatings Deposited on AZ31 Alloy Substrate, *Results Eng.,* 20, 101594(2023). https://doi.org/10.1016/j.rineng.2023.101594

Chakravarthy, V. V. K., Rajmohan, T., Vijayan, D. and Palanikumar, K., Application of Grey-ANFIS System to Optimize the Drilling Characteristics of Nano SiC Reinforced Al Matrix Composites, *Int. J. Interact. Des. Manuf.,* 17(6), 3117–3131(2023), https://doi.org/10.1007/s12008-023-01328-2

Chate, G. R., Kulkarni, R. M., Nikhil, R., Chate, V. R., Patel G. C. M., Sollapur, S. and Shettar, M., Ceramic Material Coatings: Emerging Future Applications, *Adv. Ceram. Coat. Emerging Appl.,* xxxx, 3–17(2023). https://doi.org/10.1016/B978-0-323-99624-2.00007-3

Chinnusamy, S., Ramasamy, V., Venkatajalapathy, S., Kaliyannan, G. V. and Palaniappan, S. K., Experimental Investigation on the Effect of Ceramic Coating on the Wear Resistance of Al6061 Substrate, *J. Mater. Res. Technol.,* 8(6), 6125–6133(2019). https://doi.org/10.1016/j.jmrt.2019.10.007

Deng, J., Li, C., Zhao, H., Xie, Z., Li, B. and He, J., Preparation and Tribological Performance of the Plasma-Sprayed TiWN Nano-Composite Coatings, *Constr. Build. Mater.,* 463, 140159(2025). https://doi.org/10.1016/j.conbuildmat.2025.140159

Du, F., He, L., Huang, H., Zhou, T. and Wu, J., Analysis and Multi-Objective Optimization for Reducing Energy Consumption and Improving Surface Quality during Dry Machining of 304 Stainless Steel, *Mater.,* 13(21), 4693(2020). https://doi.org/10.3390/ma13214693

Factor, M. and Roman, I., Vickers Microindentation of WC–12%Co Thermal Spray Coating, *Surf. Coat. Technol.,* 132(1), 65–75(2000). https://doi.org/10.1016/S0257-8972(00)00739-8

Feng, L., Xianliang, J., Yueguang, Y., Keli, Z., Xianjing, R. and Zhenduo, L., Preparation and Characterization of Plasma-Sprayed Ultrafine Chromium Oxide Coatings, *Plasma Sci. Technol.,* 9(1), 35–38(2007). https://doi.org/10.1088/1009-0630/9/1/08

Hango, S. I., Cornish, L. A., Merwe, J. W. V. D. and Chown, L. H., Corrosion Behaviour of a Cr_2O_3 Coating on Mild Steel in Synthetic Mine Water, *Int. J. Corros.,* 2024, 1–10(2024). https://doi.org/10.1155/2024/6343114

Hervy, T., Alroy, R. J., Björklund, S., Yao, Y., Genois, R. and Joshi, S., Evaluation of High-Throughput Columnar YSZ Thermal Barrier Coatings Deposited via Axial Plasma Spraying of Aqueous Solution Precursors, *Surf. Coat. Technol.,* 509, 132214(2025). https://doi.org/10.1016/j.surfcoat.2025.132214

Huang, D., Xue, D. L., Li, S., Niu, Y. S., Bao, Z. B., Zhu, S. L. and Wang, F. H., Performance and Failure Mechanism of Suspension Plasma-Sprayed Thermal Barrier Coatings on Smooth β-(Ni,Pt)Al Bondcoat, *Ceram. Int.,* 51(19), 28337–28350(2025). https://doi.org/10.1016/j.ceramint.2025.04.048

Jiang, J., Cui, X., Ma, G., Jin, G., Zheng, W., Liu, Y., Liu, S., Liu, M. and Wang, H., Effect of High-Temperature Oxidation on Plasma Enhanced High-Velocity Arc Spraying Inconel 625-Al_2O_3 Composite Coating, *Appl. Surf. Sci.,* 710, 164012(2025). https://doi.org/10.1016/j.apsusc.2025.164012

Kar, S., Bandyopadhyay, P. P. and Paul, S., Effect of Arc–Current and Spray Distance on Elastic Modulus and Fracture Toughness of Plasma-Sprayed Chromium Oxide Coatings, *Frict.,* 6(4), 387–394(2018). https://doi.org/10.1007/s40544-017-0166-6

Kebriyaei, A., Rahimipour, M. R. and Razavi, M., Solution Medium Suspension Plasma Spray (SMSPS): A Microstructure and High-Temperature Properties Analysis of YSZ Thermal Barrier Coating, *J. Therm. Spray Technol.,* 33(7), 2395–2407(2024). https://doi.org/10.1007/s11666-024-01848-7

Kengesbekov, A., Influence of Plasma Arc Current and Gas Flow on the Structural and Tribological Properties of TiN Coatings Obtained by Plasma Spraying, *Coat.,* 14(11), 1404(2024). https://doi.org/10.3390/coatings14111404

Kiilakoski, J., Trache, R., Björklund, S., Joshi, S. and Vuoristo, P., Process Parameter Impact on Suspension-HVOF-Sprayed Cr_2O_3 Coatings, *J. Therm. Spray Technol.,* 28(8), 1933–1944(2019). https://doi.org/10.1007/s11666-019-00940-7

Lakkannavar, V., Yogesha, K. B., Prasad, C. D., Phanden, R. K., Srinivasa, G. and Prasad, S. C., Thermal Spray Coatings on High-Temperature Oxidation and Corrosion Applications – A Comprehensive Review, *Results Surf. Interfaces.,* 16, 100250(2024). https://doi.org/10.1016/j.rsurfi.2024.100250

Liu, M., Tan, Z., Zhao, Y., Wang, H., Zhang, S., Ma, R., Jiang, T., Ma, Z., Zhong, N. and Li, W., Optimization of Spray Parameters and Corrosion Properties of Plasma-Sprayed Cr_2O_3 Coatings Using Response Surface Methodology, *Cryst.,* 15(4), 377(2025). https://doi.org/10.3390/cryst15040377

Manojkumar, P., Kalyani, B., Lakshmi, D. V., Krishna, L. R. and Sivakumar, G., Realizing Wear-Resistant Cr_2O_3 Coatings Using Finer Feedstock: Role of Diverse Plasma Spray Torch Configurations, *Ceram. Int.,* 51(18), 25960–25967(2025). https://doi.org/10.1016/j.ceramint.2025.03.279

Mao, L., Xiao, J., Sun, G., Wei, X., Wu, D., Cao, P. and Zhang, C., Microstructure and Wear Behaviors of Cr_2O_3-Al_2O_3 Composite Coatings Deposited by Atmospheric Plasma Spraying, *Surf. Coat. Technol.,* 444, 128619(2022). https://doi.org/10.1016/j.surfcoat.2022.128619

Martin, D. T., Rad, M. R., McDonald, A. and Hussain, T., Beyond Traditional Coatings: A Review on Thermal-Sprayed Functional and Smart Coatings, *J. Therm. Spray Technol.,* 28(4), 598–644(2019). https://doi.org/10.1007/s11666-019-00857-1

Mohankumar, A., Duraisamy, T., Sampathkumar, D., Ranganathan, S., Balachandran, G., Kaliyamoorthy, M., Mariappan, M. and Mulugeta, L., Optimization of Cold Spray Process Inputs to Minimize Porosity and Maximize Hardness of Metal Matrix Composite Coatings on AZ31B Magnesium Alloy, *J. Nanomater.,* 2022(1), 7900150(2022). https://doi.org/10.1155/2022/7900150

Morelli, S., Bursich, S., Bolelli, G., Puddu, P., Rossi, E., Mecca, F. G., Bortolotti, L. and Lusvarghi, L., Thermal Conductivity and Micromechanical Properties of Plasma-Sprayed Yttria-Stabilized Zirconia Thermal Barrier Coatings, *Surf. Coat. Technol.,* 513, 132498(2025). https://doi.org/10.1016/j.surfcoat.2025.132498

Nie, X., Su, H., Zhou, Y., Zhang, Z., Xu, J., Dosta, S., Rusinov, P. and Zhang, C., Effect of Hydrogen Flow Rate on Microstructure and Tribological Properties of Atmospheric Plasma Sprayed BN-Mo-NiCr Coatings, *Surf. Coat. Technol.,* 512, 132384(2025). https://doi.org/10.1016/j.surfcoat.2025.132384

Odhiambo, J. G., Li, W., Zhao, Y. and Li, C., Porosity and Its Significance in Plasma-Sprayed Coatings, *Coat.,* 9(7), 460(2019). https://doi.org/10.3390/coatings9070460

Pannerselvam, R., Design and Analysis of Experiments, *PHI Learning*, 1-576 (2012).

Patel, G. C. M., Pradeep, N. B., Girisha. L., Harsha, H. M., Shettigar, A. K., Experimental Analysis and Optimization of Plasma Spray Parameters on Microhardness and Wear Loss of Mo-Ni-Cr Coated Super Duplex Stainless Steel, *Aust. J. Mech. Eng.,* 20(5), 1426–1438(2022). https://doi.org/10.1080/14484846.2020.1808760

Prashar, G., Thakur, K., Singh, S., Singh, P. and Kumar, S., Microstructural Characterization of Plasma Sprayed Chromium Oxide Coating on SS-310 Steel, *AIP Conf. Proc.,* 2986, 020001(2024). https://doi.org/10.1063/5.0192481

Samal, S., Zeman, J., Habr, S., Pacherová, O., Chandra, M., Kopeček, J. and Šittner, P., Evaluation of Microstructure–Porosity–Hardness of Thermal Plasma-Sprayed NiTi Coating Layers, *J. Manuf. Mater. Process.,* 7(6), 198(2023). https://doi.org/10.3390/jmmp7060198

Schino, A. D., Manufacturing and Application of Stainless Steels, *MDPI – Multidiscip. Digital Publ. Inst.,* 10(3), 327(2020). https://doi.org/10.3390/met10030327

Shabani, C. Z., Abdollah-zadeh, A., Seraj, R. A., Azarniya, A., Effect of Cold Spray Processing Parameters on the Microstructure, Wear, and Corrosion Behavior of Cu and Cu–Al2O3 Coatings Deposited on AZ31 Alloy Substrate, *Results Eng*., 20, 101594 (2023). https://doi.org/10.1016/j.rineng.2023.101594

Sun, X., Zhang, W., Shang, X., Chen, S., Song, C. and Zhang, L., Microstructure, Reaction Mechanism, and Properties of in-Situ Submicron TiC and Nano-TixO Particle-Reinforced Cu-Based Composite Coatings Prepared through Simultaneous Solid-Solid and Solid-Gas Reactive Plasma Spraying, *Surf. Interfaces.,* 72, 107138(2025). https://doi.org/10.1016/j.surfin.2025.107138

Thilagashanthi, T., Gunasekaran, K. and Satyanarayanan, K. S., Microstructural Pore Analysis Using SEM and ImageJ on the Absorption of Treated Coconut Shell Aggregate, *J. Clean. Prod.,* 324, 129217(2021). https://doi.org/10.1016/j.jclepro.2021.129217

Thirugnanasambandam, A., Gupta, M. and Mariyadas, A., Corrosion Resistance and Wear Response of Plasma Spray Nano-Ceramic Composite Coatings on AZ91D Alloy, *J. Mater. Eng. Perform.,* 34(13), 12469–12484(2025). https://doi.org/10.1007/s11665-024-10021-8

Vakili, M., Koutník, P., Kohout, J. and Gholami, Z., Analysis, Assessment, and Mitigation of Stress Corrosion Cracking in Austenitic Stainless Steels in the Oil and Gas Sector: A Review, *Surf.,* 7(3), 589–642(2024). https://doi.org/10.3390/surfaces7030040

Vaßen, R., Kalfhaus, T., Vorkötter, C., Sohn, Y. J., Conze, S. and Berger, L. M., Atmospheric Plasma Spraying of Different MgO/Al_2O_3 Feedstocks, *J. Therm. Spray Technol.,* 32(2-3), 514–522(2023). https://doi.org/10.1007/s11666-023-01541-1

Xiong, W., Ma, M., Zhang, J. and Lian, Y., The Effects of Cr_2O_3 Particles on the Microstructure and Wear-Resistant Properties of Electrodeposited CoNiP Coatings, *Surf. Coat. Technol.,* 381, 125167(2020). https://doi.org/10.1016/j.surfcoat.2019.125167

Zhang, J. T., Analysis of Variance for Functional Data; Chapman & Hall/CRC Monographs on Statistics and Applied Prob Series, 1st Ed., CRC Press LLC, 1-412(2024). https://doi.org/10.1201/b15005

Zhou, C., Gong, C., Liu, Q., Hao, Z., Xu, Z. and Tian, X., Research on Micro-Nanoscale SiCp/6061Al Composite Coating Using High-Pressure Cold Spray, *J. Therm. Spray Technol.,* 33(8), 2815–2826(2024). https://doi.org/10.1007/s11666-024-01880-7

Zhou, C., Gong, C., Xu, Z., Liang, T., Liu, Q., Liu, Y., Hao, Z., Lin, C., Liu, J. and Tian, X., Effect of Solution Treatment on Hardness and Tribological Properties of Micro-Nano SiCp/6061Al Coatings Fabricated by Cold Spray, *J. Manuf. Processes.,* 149, 697–708(2025). https://doi.org/10.1016/j.jmapro.2025.06.